Shape- and excitation-dependent charge-carrier dynamics in colloidal MAPbI perovskites as nanostripes, nanosheets and nanoplatelets

Eugen Klein,[1] Chris Rehhagen,[1] Rostyslav Lesyuk,[1,2] Christian Klinke[1,3,4]*

[1] *Institute of Physics, University of Rostock, Albert-Einstein-Strasse 23, 18059 Rostock, Germany*
[2] *Pidstryhach Institute for applied problems of mechanics and mathematics of NAS of Ukraine, Naukowa str. 3b, 79060 Lviv, Ukraine*
[3] *Department "Life, Light & Matter", University of Rostock, Albert-Einstein-Strasse 25, 18059 Rostock, Germany*
[4] *Department of Chemistry, Swansea University – Singleton Park, Swansea SA2 8PP, United Kingdom*
* Corresponding author: christian.klinke@uni-rostock.de

Abstract

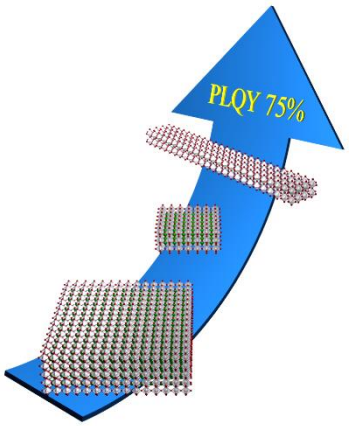

Nanostructured lead halide perovskites are an attractive group of materials for highly efficient optoelectronic applications. Considering the wide variety in shape, size and crystal structures (layered, non-layered, hollow, double), many different excited-state population and relaxation processes can be present, such as exciton formation, free charge carrier generation, exciton-exciton annihilation, and Auger recombination. Here, we present the synthesis of nanostructures with different morphology to improve the optical properties of methylammonium lead iodide and to investigate the corresponding charge-carrier dynamics and recombination processes. Excitation intensity dependent time-resolved photoluminescence (PL) measurements are performed to highlight the PL decay behaviour of nanosheets, nanoplatelets, and nanostripes. In all three cases a faster decay rate is observed with increasing excitation fluence. This behaviour can be attributed to the occurrence of bimolecular recombination of electrons and holes in nanosheets and exciton-exciton annihilation in nanostripes with high carrier densities. Performing these measurements at low excitation intensities revealed unusual long charge-carrier lifetimes of a few microseconds. Additionally, the nanostripes showed the best results in terms of photoluminescence quantum yield of up to 75 % and the nanosheets demonstrate improved stability. The nanoplatelets are considered as intermediate structures between nanosheets and nanostripes – balancing quantum yield and stability.

Key words: colloidal synthesis, methylammonium lead iodide, nanostructures, spectroscopy, exciton-exciton annihilation

Introduction

Organic-inorganic metal halide perovskites have emerged as promising materials for realizing highly efficient optoelectronic applications such as lasers, photovoltaic devices and light-emitting diodes [1–4]. Size and morphology control, influencing confinement and dimensionality [5], have demonstrated further fields of application of these materials [6–9]. Out of these structures nanocrystals and their control in thickness and lateral dimensions have been intensively investigated in the recent years [10,11]. While pursuing the goal of preparing materials with higher efficiencies for applications like photovoltaics, it is vital to understand the fundamental physics of carrier generation and relaxation processes in such systems. Auger recombination or exciton-exciton annihilation (EEA) are non-linear processes at higher carrier densities which are unfavourable to device functionality and thereby limiting emission intensity and efficiency [12–16]. The reduced dimensionality in one or more directions can favor these many-body interactions of excitons and free charge carriers and significantly reduce the photoluminescence quantum yield (PLQY) [17–20].

In this work, we present the synthetic ways to switch the shape of MAPbI perovskite nanostructures and describe related optical properties such as PL spectra, life time and quantum yield. We prepared three types of such MAPbI structures: nanosheets, nanoplatelets and nanostripes. All three types of nanomaterials have a non-layered crystal structure. Investigating the PLQY, we found that the nanoplatelet and nanostripe structures exhibit an immense improvement compared to nanosheets, while the nanostripes excel even the platelets. On the other hand, all three types of perovskites show a similar unusual long PL lifetime behaviour – in the range of microseconds. This behaviour is highly dependent on the excitation intensity due to strong bimolecular recombination of the charge carriers and EEA at elevated fluences. Here, the nanostripe morphology exhibits the strongest effect of excitation power on the PL lifetime compared to nanoplatelets and nanosheets. This non-linear behavior promotes PL lifetimes in the order of a few nanoseconds at higher fluences while performing these measurements at low excitation intensities reveals values of a few microseconds. These results give insights into the nature of the charge carriers and bimolecular processes in non-layered colloidal lead iodide perovskites and suggest potential applications of differently shaped structures.

Results and Discussion

The MAPbI nanostructures discussed here were synthesised through a modified hot injection method reported previously by our group [21]. This method comprises two steps: one for the preparation of the lead iodide precursor [22] and one for the formation of the perovskite materials. The precursors already have quasi-2D shape with a distinct ligand shell and are getting dissolved into small nanoparticles and ions. This is followed by a hot-injection of the methylammonium iodide (MAI) precursor and the formation of the perovskite structures. The three types of particles compared here were synthesised at

similar parameters with one difference for each of them with hexadecylamine (HDA) as the main ligand. Nanostripes were prepared with 4 mL of the solvent diphenylether (DPE) and a procedure where the MAI precursor is injected at the reaction temperature of 90 °C. The nanoplatelets were synthesized in the same way but with 5 mL of DPE. The formation of the nanosheets was performed at an injection temperature for the MAI precursor of 32 °C and a subsequent slow increase of the temperature to 90 °C with 4 mL of DPE. The nanosheets depicted in Figure 1a have a smooth surface and straight edges with lateral dimensions between 0.2 µm and 2 µm and the shape varies between squares and rectangles. The nanoplatelets have a size distribution of 100 nm to 300 nm in the lateral dimensions with uneven edges and surfaces (Figure 1b). On the other hand, the nanostripes are even in surface and edges and show a size distribution between 0.1 µm and 7 µm in length and 5 nm to 100 nm in width (Figure 1c). The polydispersity of all three structures is presented in Figure S1. The insets in Figure 1a–c show corresponding selected area electron diffraction (SAED) patterns for all three types of MAPbI nanostructures. All show a dot pattern – indicating the single-crystal nature of the individual particles. The materials have the same tetragonal crystal structure with a space group of I4/mcm and lattice constants $a = b = 8.85$ Å and $c = 12.64$ Å determined from X-ray diffraction (XRD) patterns for MAPbI (Figure 1d and Figure S2) which agrees well with the reference pattern. Some of the peaks are missing or supressed due to a strong texture effect resulting from the preferred planar orientation of the nanostructures on the XRD wafer [23].

Out of these three types, the challenge was the preparation of the nanostripes with an additional restriction in one of the lateral dimensions. These nanoparticles were only accessible at conditions with high concentrations of reactants and a reaction temperature of 90 °C. Performing the synthesis at lower concentrations yielded solely nanoplatelets or a mixture of undefined particles as products (Figure S3). Reactions with similar or less concentrations but with a different synthesis method produced nanosheets as products (Figure S4). Since the reactivity of this synthesis is very high at 90 °C, nucleation and growth takes place immediately upon injection of the second reactant. This means that all of the second precursor reacts near the area of the injection and gets distributed by the stirring afterwards. This leads to a high shape and size distribution at lower reactant concentrations. In contrast, reactions with an injection temperature of 32 °C and a slow increase to the reaction temperature of 90 °C yield solely nanosheets as products due to a homogeneous distribution of both reactants prior to the nucleation. Here, the decrease in concentration results in nanosheets with smaller lateral dimensions. Additionally, we varied other parameters like temperature, amine amount, and ratio of the reactants to verify the range for the formation of the nanostripes. Unfortunately, such changes lead to the formation of particles with different morphologies and reduced the amount of nanostripes in the corresponding syntheses (Figure S5).

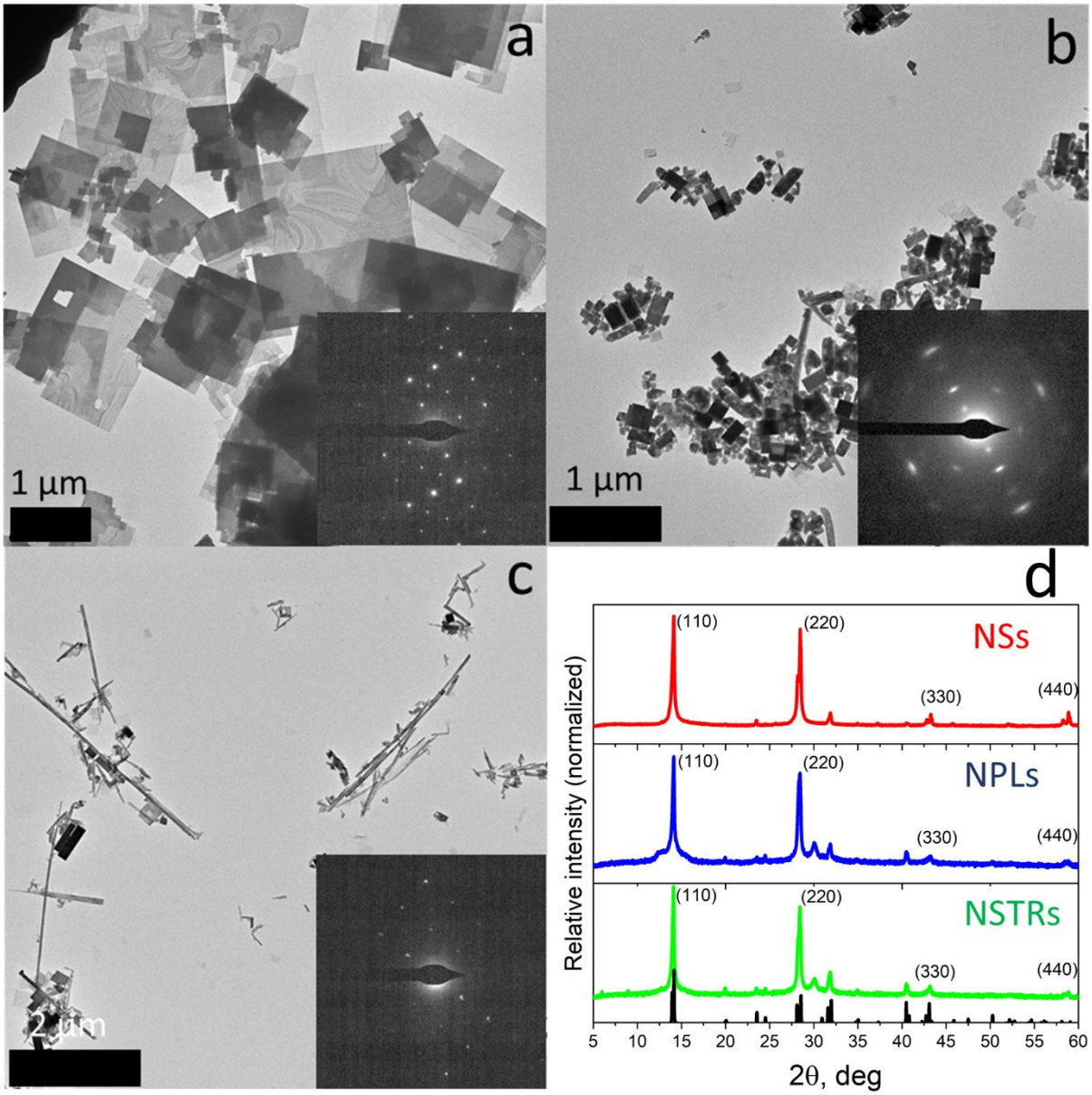

Figure 1. Bright field TEM images of MAPbI nanosheets (NSs, a), nanoplatelets (NPLs, b), and nanostripes (NSTRs, c). The insets show SAED patterns of the corresponding type of perovskite material. (d) XRD patterns of the MAPbI structures. Black pattern represent the reference $MAPbI_3$ XRD reflections calculated according to [24].

Figures 2a-c show atomic force microscopy (AFM) images with the corresponding height profiles for all three structures. The thickness of the nanosheets ranges between 20 nm and 200 nm, for nanoplatelets between 50 nm and 300 nm and for nanostripes between 4 nm and 60 nm. The strong distribution in thickness is a result of the high concentration of the reactants and the reaction temperature. These parameters favour the formation of bulk, non-layered structures. The non-layered structures are individual crystals while the layered structures are close-packed well-arranged objects consisting of these single individual crystals connected in most cases via ligands that exhibit double ligand formation. In most of the preparation methods in literature the perovskites are synthesized at low temperatures (room temperature) and as a result layered materials are formed. In our case, with 90 °C the reaction

temperature is higher and is the main reason for the formation of non-layered structures. Due to the higher temperature and therefore higher molecular motion the spacer ligands are not able to form stable double ligand formation which leads to single crystals. UV-vis absorption and PL spectra of the discussed materials are presented in Figures 2d-f with their optical features close to the infrared region. While the nanoplatelets and nanostripes show identical absorption band edges at 765 nm and sharp emission peaks at 766.5 nm, a clear red shift of the absorption edge and PL maximum is present for the nanosheets being observed at 768.5 nm for absorption and 770 nm for PL. The origin of the broad absorption region around 500 nm is still in discussion and may stem from the transition from the second highest valence band (VB2) to the lowest conduction band (CB1) minimum or PbI_2 residuals in the perovskite products among others [25–29].

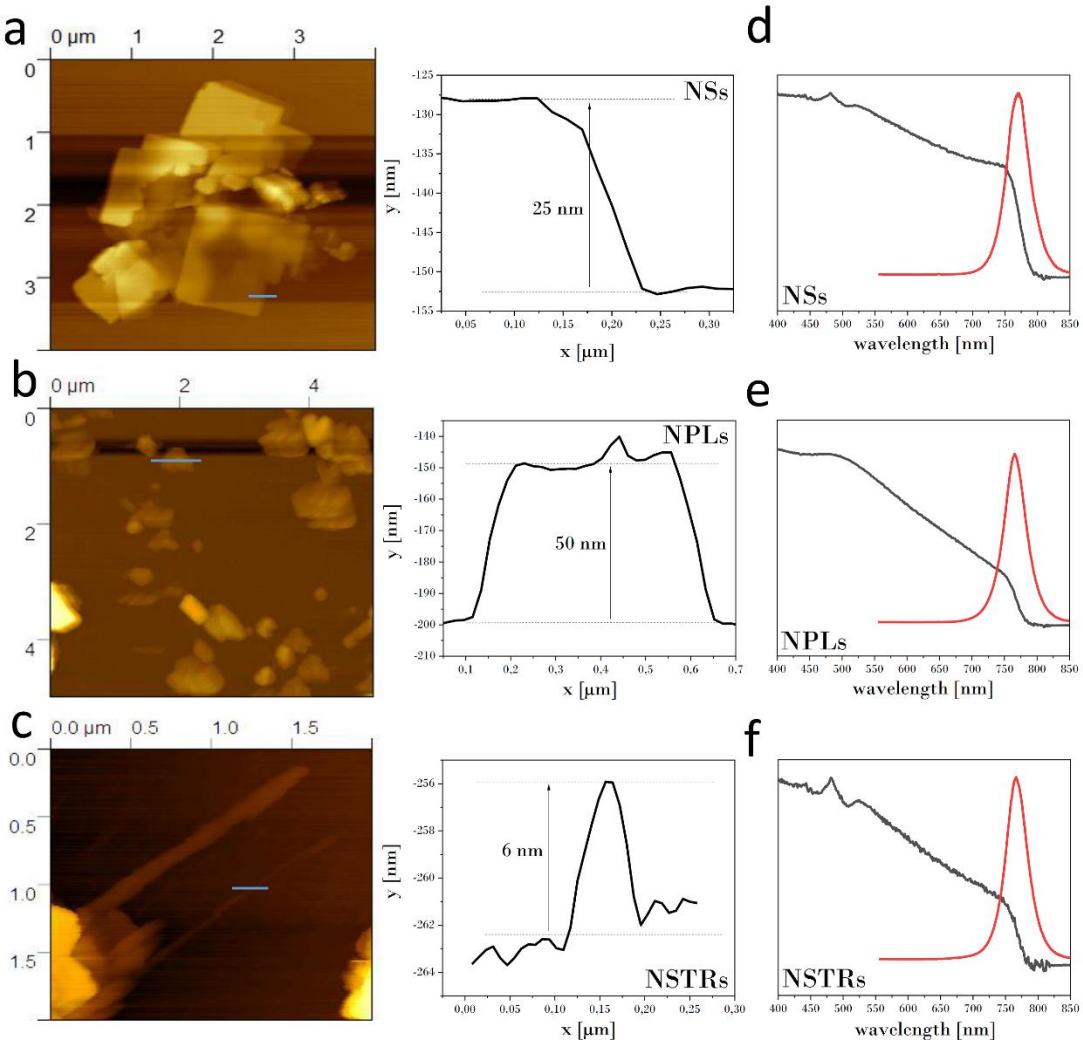

Figure 2. AFM images of $MAPbI_3$ nanosheets (a), nanoplatelets (b), and nanostripes (c) with corresponding height profiles. UV-vis absorption (black) and emission (red) spectra (d-f) of the three corresponding nanoparticle types.

The presented three types of MAPbI nanostructures show similar symmetric, narrow steady-state PL spectra – but they differ substantially in quantum yield and stability. The nanosheets show relatively low quantum yield (about 10%) in comparison to the nanoplatelets (30%) and the nanostripes (75%)

measured at very low excitation level conditions in solution (Figure S6). However, latter suffer from reduced stability. In contrast, the nanosheets are quite stable – also under a fluence of above 100 μJ/cm^2. We studied the PL properties in time-resolved mode to shed light onto possible photo-physical processes in these nanostructures and to get information about actual lifetimes of charge carriers and their nature. The nanocrystals discussed here show no layered stacking behavior and are not in strong confinement being rather 3D nanocrystals with strongly anisotropic 2D geometry. Despite this, a certain degree of spatial confinement due to the geometry and intense excitation promote electron-hole interaction and the existence of excitons along with free charge carriers at room temperature [30]. During the attempts to quantify the PL lifetime (τ) for the three discussed types of nanostructures, we noticed a strong dependency of the effective lifetime on the excitation fluence. In Figure 3, the PL decays are shown for representative nanosheets, nanoplatelets, and nanostripes in the range of 0.2 to 105 μJ/cm^2 under a focused laser beam with the wavelength of 440 nm in a confocal fluorescence-lifetime imaging microscope (FLIM) at ambient conditions on a glass substrate. The obtained average lifetimes are in the range of tens to hundreds of nanoseconds. However, the upper limit of the lifetime could not be reached by decreasing the excitation fluence (Figure 4). This picture suggests a strong recombination acceleration with the fluence already observed previously for free charges and excitons in literature [24,31-38]. For excitons in the bimolecular interaction regime, this effect is known as exciton-exciton annihilation or biexciton Auger process [12,20,39]. It represents intrinsic physical constraint for the quantum efficiency of lead-based halide perovskite optoelectronic devices. Relaxation through bimolecular pathways, in particular through non-geminate electron-hole recombination, is obviously enhanced in low-dimensional systems such as nanocrystals and nanosheets due to volumetric constraints [40,41] and surface effects [42] and might contribute to the PL kinetics in our samples. However, the dependence of the EEA rate on the spatial confinement is rather complex and ambiguous [43] involving reaction radius of the annihilation process, trapping and de-trapping of excitons [38], mobility and the exciton lifetime [31]. A qualitative indicator of the progressive bimolecular process in our case is the character of decays at intermediate excitation fluences, depicted in Figure S7. The decays can be fitted by rate equation with mono-molecular and bimolecular terms (equation 1 and 2 in SI). Initially the fit quality is low and increases with excitation fluence, however, at the highest excitation level the fit becomes worse again in NSTRs and NPLs suggesting further mechanisms involved such as Auger three-body interaction for example. For NSs, the fitting shows that the recombination dynamics is governed by the bimolecular process only at higher levels (best fit at the maximal excitation intensity) in contrast to NPLs and NSTRs.

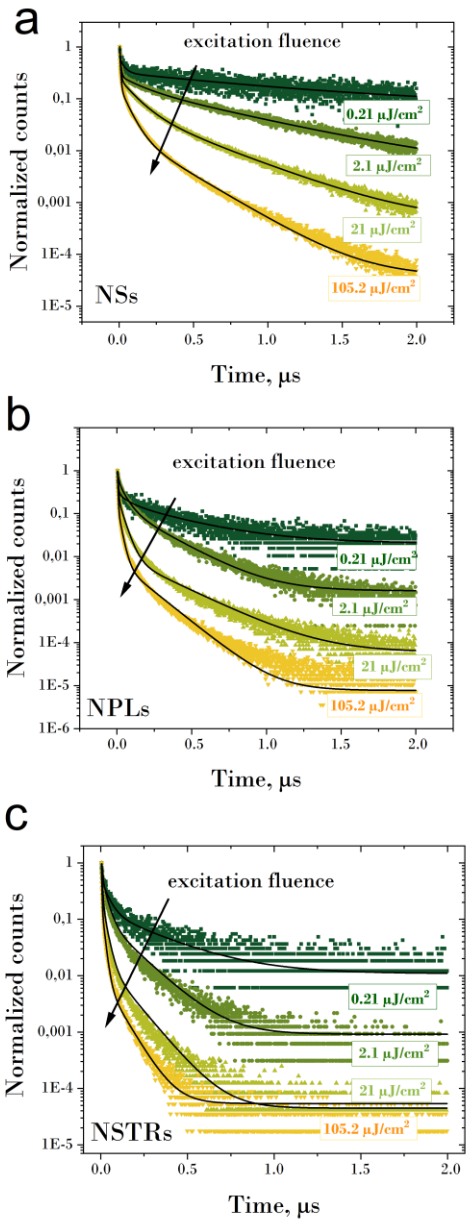

Figure 3. Excitation fluence-dependent PL decays under focused laser beam of representative individual nanocrystals: nanosheet (NS, a), nanoplatelet (NPL, b) and nanostripe (NSTR, c) by 0.21 μJ/cm², 2.1 μJ/cm², 21 μJ/cm² , and 105 μJ/cm² excitation energy density. Three-exponential fits are plotted as black lines.

To characterize the nature of the charge carriers participating in the bimolecular recombination processes, we plot the PL intensity at the maximum of each decay trace (at zero time) versus excitation fluence in a double-logarithmic plot. Fitting the trend with the power function $PL_0 = a \cdot E^b$ (Figure 5) indicates the monomolecular recombination with b to be close to 1.0 at low fluences and further slowing (non-linearity) of the trend ($b \approx 0.6…0.8$), however for nanosheets b is slightly larger than 1.0. Since initially $b \approx 1$ in nanostripes and nanoplatelets, excitons should dominate in these excited perovskite nanocrystals [43,44]. Inclination of the trend to the power function with $b < 1$ can then be referred to progressive EEA. A further important indicator for the type of bimolecular recombination is PL quantum yield (PLQY). If bimolecular recombination of electrons and holes is dominant, the PLQY must

increase [41], while for the Auger recombination including EEA, the PLQY should decrease with excitation intensity [35]. Despite the difficulties finding the absolute PLQY for nanocrystals in FLIM configuration, the relative QY trend was followed by dividing PL_0 by the excitation fluence and plotting it versus the incoming fluence (Figure 5d). We note that for the nanosheets the PLQY increases with the excitation fluence, while for the nanostripes and the nanoplatelets it decreases. This gives us another indication that in nanosheets bimolecular recombination of electrons and holes takes places while in nanoplatelets and especially in nanostripes, rather EEA might be responsible for the observed lifetime decrease with excitation fluence.

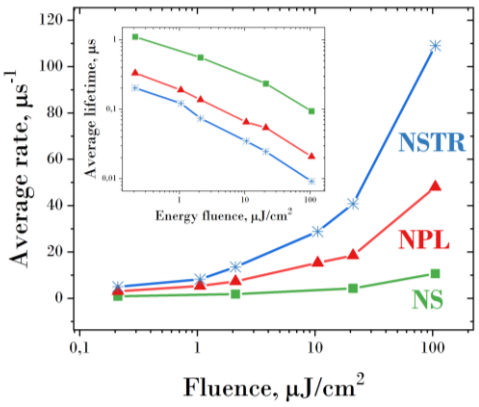

Figure 4. Intensity-weighted average rates and corresponding average PL lifetimes for representative nanosheets, nanoplatelets and nanostripes in FLIM configuration obtained by variable energy fluence (from 0,2 to 105 µJ/cm^2) as function of the excitation fluence.

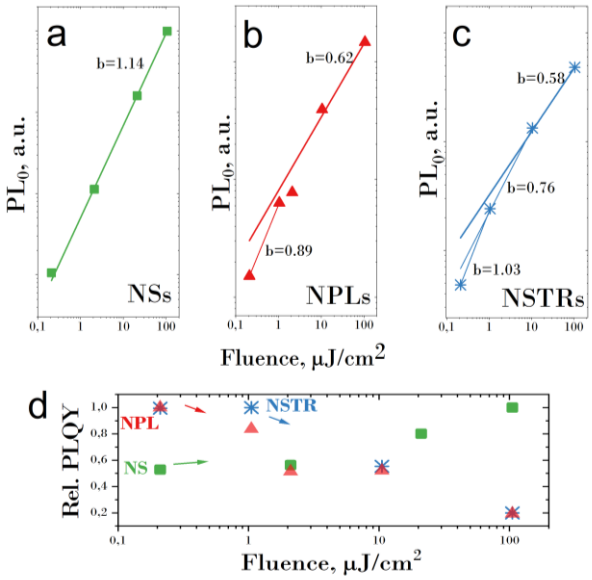

Figure 5. Plots of PL_0 as function of the excitation fluence *E* in FLIM measurements for representative nanosheets (a), nanoplatelets (b) and nanostripes (c). Fit with the power law $PL_0 = a \cdot E^b$ where the exponent determines the recombination mechanism [44]. (d) Relative PLQY for excitation fluences from a, b, and c for nanosheets (green), nanoplatelets (red), and nanostripes (blue).

To follow the PL kinetics towards longer lifetimes with further decreasing excitation fluence, additional measurements were performed in solution with much lower excitation energies within a commercial PL spectrometer (see Experimental section). Despite the sensitivity of hybrid perovskites to the environment [45], light treatment of traps [45,46] and surface chemistry [47], we were able to observe distinct similarities between the two types of measurements – in ensemble (solution) and on single particles as well as some differences. The measurements in solution showed further increase of the average lifetimes with decreasing excitation intensity for all three types of nanomaterials (Figure S8) and average lifetimes in the order of microseconds. This indicates that in our MAPbI nanocrystals the bimolecular effects play a prominent role in the relaxation kinetics for a large range of excitation energies and that the intrinsic lifetimes of the charge carriers are in fact very large. Similar to the FLIM

analysis, we analyzed the decay traces with 3-exponential fits and kept τ_1, τ_2, τ_3 as global parameters. The average lifetimes for the three modifications of MAPbI (Figure 6) with corresponding average decay rates change (Figure S9) were determined. Interestingly, in the lowest excitation range the lifetimes initially increase with the excitation fluence, then saturate and eventually start to decrease. The increase of the lifetime at the beginning stems from the fast component with the time constant of 28 ns and 34 ns for nanoplatelets and nanostripes and 264 ns for nanosheets. Important is that the fractional contribution of this component gradually decreases with the excitation upon a certain limit after which it starts increasing (Table S1). We attribute the initial fast component at low excitation fluences to the relaxation through non-radiative recombination centers (NRC) [35,36,43,48] which might be surface traps in our case. After the NRCs are filled, the lifetime is saturated and in case of NSTRs due to the high PLQY shows the intrinsic radiative lifetime of charge carriers. Further, the acceleration of the decay beyond this point indicates that the MAPbI structures enter the bimolecular recombination regime. This is supported by the relative QY for nanocrystals in the low-excitation mode (Figure S10). For nanosheets and nanoplatelets, we observe an increase of the relative QY throughout the whole range (NRC saturation), while for the nanostripes this parameter increases and then saturates – indicating the onset to EEA. We note that the colloidal solution of NSTRs contains some residual amount of NPLs as side product that slightly influences the trend of relative QY of NSTRs vs fluence. Here, we can conclude that excitation and relaxation in nanoplatelets is governed mainly by free electrons and holes along with excitons. So, they represent an intermediate regime between nanosheets and nanostripes which is supported also by the absolute PLQY and the stability behavior.

From the results of the ensemble measurements, we note that nanoplatelets and nanostripes show the fastest decays and nanosheets the slowest. Based on the fitting results, we carefully state that the corresponding intrinsic lifetimes are in the range of **1.3 µs, 2 µs, and 8–9 µs for nanoplatelets, nanostripes, and nanosheets**, respectively. These values are relatively high in comparison to the lifetimes reported for 0D, 2D and some 3D MAPbI perovskites [25,49,50] which are usually in the range of tens and hundreds of ns and are comparable with values for MAPbI-based perovskites with long diffusion lengths [4,51]. We note that the slowest behavior is observed for nanosheets both in low- and high excitation regime, whereby nanostripes and nanoplatelets show much faster relaxation. Nanostripes in turn show faster relaxation than nanoplatelets at higher excitation fluences (FLIM configuration) and demonstrated the fastest trend regarding EEA with respect to the excitation fluence. Ma *et al.* reported a similar trend in behavior for $(C_6H_{13}N_4)_3Pb_2Br_7$ 1D assemblies [31]. However, in our case in the linear-log representation in Figure 4, non-linear behavior is observed, where the charge-carrier recombination is accelerated at higher excitations suggesting an involvement of additional mechanisms (such as third-order Auger effects).

We also note that nanosheets leave the NRC-saturation range and enter into the bimolecular relaxation mode at lower excitations than nanoplatelets and nanostripes. At the same time, NSs show relatively

low QY. These observations reveal extremely long radiative lifetimes of charge carriers in nanosheets and pronounced bimolecular relaxation process with increasing excitation fluence. The lower quantum yield of nanosheets can be explained by the existence of several slow non-radiative channels which might be responsible for the microsecond components and can stem from intrinsic trap states for charge carriers. This is supported by a slight shift of the PL maximum of nanosheets in comparison to NSTRs and NPLs. NPLs and NSTRs in turn stay longer in NRC-saturation regime due to less pronounced bimolecular processes in the ensemble measurement and a seemingly larger amount of surface traps due to a larger surface-to-volume ratio.

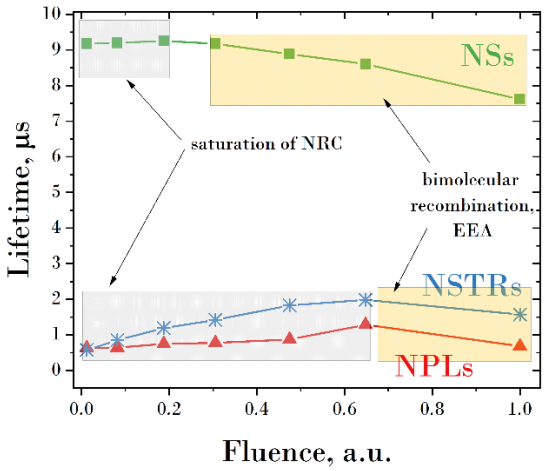

Figure 6. Intensity-weighted average lifetime of nanosheets, nanostripes, and nanoplatelets in ensemble in low-excitation regime as a function of the excitation fluence.

A further look at the three components contributing to the decay kinetics of the nanocrystals at different excitation fluence in regard to EEA or free charge carriers recombination, we find that the fractions of the long µs-components progressively decrease and eventually almost completely disappear at higher excitation fluences (FLIM mode) whereby only ns-components contribute to the PL decays. Apparently, the µs-relaxation channels in nanoplatelets, nanostripes, and nanosheets are related to the long-living excited states, which cannot be reached (populated) in the high-excitation mode leading to a strong contribution of bimolecular recombination. Relaxation through the EEA mechanism outcompetes the intrinsic durable excitonic recombination, especially pronounced in nanostripes. We speculate that the geometry of nanosheets is more suitable for the lasting charge-carrier migration. However, the non-radiative channels play a dominant role in these nanostructures since a relatively low PLQY is observed by different excitations. In nanoplatelets and especially in nanostripes the QY is higher – reaching ~75% for nanostripes, which is indicative for the formation of excitonic states with higher radiative rates. One can attribute this to the spatial confinement regime implying also more intensive light absorption. Having less volume per absorbed photons, the nanostripes and nanoplatelets should be more prone to Auger decay and the EEA effect particularly [1,17]. The nature of long-living PL in halide perovskites is actively debated and was referred to different phenomena such as Rashba spin-orbit coupling and

spin-forbidden transitions [52], indirect spin-split band-gap [53], localization in large polarons [54,55] and trapping-detrapping processes with delayed phololuminescence [38]. We note that further studies are necessary to disentangle the mechanism behind the long PL lifetimes in detail in our system with three different morphologies. Usually, the long PL lifetime in hybrid organic-inorganic perovskites is associated with large charge-carrier diffusion lengths and can be advantageous for steady-state population accumulation under excitation. This in turn opens perspectives for applications of differently shaped MAPbI nanostructures in solar cells and low-threshold cw lasing devices.

Conclusion

We demonstrated synthetic routes for three spatial modifications of MAPbI perovskite: nanosheets, nanoplatelets, and nanostripes, based on a two-step synthesis procedure. In particular, the nanostripes were only accessible in a narrow set of parameters where the second precursor was injected at the reaction temperature and the concentration of the reactants was high. The length of these nanostripes can be more than 7 µm while the width is restricted to at max. 100 nm. All three materials show a non-layered stacking behavior with PL maxima in the bulk regime. Thin nanostripes show very high quantum yield of about 75%, while nanoplatelets and nanosheets demonstrate better stability. All three modifications have charge-carrier lifetimes in the µs range, whereby the nanosheet morphology promotes PL lifetimes of up to 9 µs in solution. All advanced properties could not be combined in one nanostructure so far. High quantum yield of nanostripes comes with a deterioration in stability, which is a problem known in literature and long exciton lifetimes are suppressed by a second-order effect such as exciton-exciton annihilation or bimolecular free charge-carrier recombination for all the nanostructures. However, the obtained morphologies with different combinations of optical properties demonstrate the variety of choice for perspective optoelectronic applications.

EXPERIMENTAL SECTION

Chemicals and reagents. All chemicals were used as received: Lead(II) acetate tri-hydrate (Aldrich, 99.999%), oleic acid (OA, Aldrich, 90%), tri-octylphosphine (TOP; ABCR, 97%), 1,2-diiodoethane (DIE; Aldrich, 99%), methylammonium iodide (MAI; Aldrich, 98%), diphenyl ether (DPE; Aldrich, 99%), toluene (VWR, 99,5%), dimethylformamide (DMF; Aldrich, 99,8%), hexadecylamine (HDA; Aldrich, 90%), dodecylamine (DDA; Merck, 98%), tetradecylamine (TDA; Merk, 98%).

PbI_2 nanosheet synthesis. In a typical synthesis a three neck 50 mL flask was used with a condenser, septum and thermocouple. 860 mg of lead acetate tri-hydrate (2.3 mmol) were dissolved in 20 mL of

oleic acid (60 mmol) and heated to 80 °C until the solution turned clear in a nitrogen atmosphere. Then vacuum was applied to remove the acetic acid which is generated by the reaction of oleic acid with the acetate from the lead precursor. After 1.5 h the reaction apparatus was filled with nitrogen again and 2 mL of a 48.7 mg 1,2-diiodoethane (0.17 mmol) in 3 mL oleic acid precursor was added at 80 °C to the solution. After 4 minutes 0.06 mL of tri-octylphosphine (TOP) (0.13 mmol) was added to the reaction solution. After 8 minutes the heat source was removed and the solution was left to cool down below 60 °C. Afterwards, it was centrifuged one time at 4000 rpm for 3 minutes. The particles were suspended in 11.5 mL toluene and put into a freezer for storage.

Synthesis of $MAPbI_3$ nanosheets. A three neck 50 mL flask was used with a condenser, septum and thermocouple. 4 mL of diphenyl ether (25.1 mmol), 0.42 mL of a 400 mg hexadecylamine (1.66 mmol) in 4 mL diphenyl ether precursor were heated to 80 °C in a nitrogen atmosphere. Then vacuum was applied to dry the solution. After 1.5 h the reaction apparatus was filled with nitrogen again and 2 mL of as prepared PbI_2 nanosheets in toluene were added. The temperature was reduced to 32 °C following the dissolution of PbI_2. The synthesis was started with the injection of 0.06 mL of a 600 mg methylammonium iodide (3.77 mmol) in 6 mL dimethylformamide precursor. The temperature was slowly increased to 90 °C over a period of 6 minutes right after the injection. The heat source was removed at 90 °C and the solution was left to cool down below 60 °C. Afterwards, it was centrifuged at 4000 rpm for 3 minutes. The particles were washed two times in toluene before the product was finally suspended in toluene again.

Synthesis of $MAPbI_3$ nanoplatelets. A three neck 50 mL flask was used with a condenser, septum and thermocouple. 5 mL of diphenyl ether (31.4 mmol), 0.1 mL of a 500 mg dodecylamine (2.70 mmol) in 4 mL diphenyl ether precursor and 0.4 mL (1.62 mmol) of TBP were heated to 80 °C in a nitrogen atmosphere. Then vacuum was applied to dry the solution. After 1.5 h the reaction apparatus was filled with nitrogen again, the temperature was increased at 220 °C and 2 mL of as prepared $PbCl_2$ nanosheets in toluene was added. After all of the $PbCl_2$ was dissolved the temperature was reduced to 140 °C. The synthesis was started with the injection of 0.4 mL of a 50 mg methylammonium chloride (0.74 mmol) in 6 mL dimethylformamide precursor. After 5 minutes the heat source was removed and the solution was left to cool down below 60 °C. Afterwards, it was centrifuged at 4000 rpm for 3 minutes. The particles were washed two times in toluene before the product was finally suspended in toluene again.

Synthesis of $MAPbI_3$ nanostripes. A three neck 50 mL flask was used with a condenser, septum and thermocouple. 4 mL of diphenyl ether (25.1 mmol), 0.42 mL of a 400 mg hexadecylamine (1.66 mmol) in 4 mL diphenyl ether precursor were heated to 80 °C in a nitrogen atmosphere. Then vacuum was applied to dry the solution. After 1.5 h the reaction apparatus was filled with nitrogen again, the temperature was raised to 90 °C and 2 mL of as prepared PbI_2 nanosheets in toluene were added. The synthesis was started with the injection of 0.06 mL of a 600 mg methylammonium iodide (3.77 mmol) in 6 mL dimethylformamide precursor. After 1.5 minutes the heat source was removed and the solution

was left to cool down below 60 °C. Afterwards, it was centrifuged at 4000 rpm for 3 minutes. The particles were washed two times in toluene before the product was finally suspended in toluene again.

Characterization. The TEM samples were prepared by diluting the nanostripe suspension with toluene followed by drop casting 10 µL of the suspension on a TEM copper grid coated with a carbon film. Standard images were done on a Talos-L120C and EM-912 Omega with a thermal emitter operated at an acceleration voltage of 120 kV and 100 kV. X-ray diffraction (XRD) measurements were performed on a Panalytical Aeris System with a Bragg-Brentano geometry and a copper anode with a X-ray wavelength of 0.154 nm from the Cu-kα1 line. The samples were measured by drop-casting the suspended nanostripes on a <911> or <711> cut silicon substrate. Atomic force microscopy (AFM) measurements were performed with AFM from Park Systems XE-100 in non-contact mode. UV/vis absorption spectra were obtained with a Lambda 1050+ spectrophotometer from Perkin Elmer equipped with an integration-sphere. The PL spectra measurements were obtained by a fluorescence spectrometer (Spectrofluorometer FS5, Edinburgh Instruments) for ensemble samples (in toluene). For the time-resolved PL measurements, a picosecond laser with 375 nm excitation wavelength and 100 kHz repetition rate was used and ≈0,004 µJ/cm^2 energy density per pulse. The decay profiles are tail-fitted with a tri-exponential function $R(t) = A_1 \exp\left(-\frac{t}{\tau_1}\right) + A_2 \exp\left(-\frac{t}{\tau_2}\right) + A_3 \exp\left(-\frac{t}{\tau_3}\right)$, and the average PL lifetime is calculated using the formula $\tau_{average} = \frac{A_1\tau_1^2 + A_2\tau_2^2 + A_3\tau_3^2}{A_1\tau_1 + A_2\tau_2 + A_3\tau_3}$. PLQYs of the samples were measured using an absolute method by directly exciting the sample solution and the reference (toluene in our case) in an SC-30 integrating sphere module fitted to a Spectrofluorometer FS5 from Edinburg Instrument. During the measurement, the excitation slit was set to 6.5 nm, and the emission slit was adjusted to obtain a signal level of 1×10^6 cps, the excitation wavelength was chosen to 530 nm with ≈50 µW/cm^2 irradiance (few orders of magnitude lower than in confocal measurements). A wavelength step size of 0.1 nm and an integration time of 0.2 s were used. The calculation of absolute PL QY is based on the formula, $\eta = \frac{E_{sample} - E_{ref}}{S_{ref} - S_{sample}}$, where η is absolute PL QY, E_{sample} and E_{ref} are the integrals at the emission region for the sample and the reference, respectively, and S_{sample} and S_{ref} are the integrals at the excitation scatter region for the sample and the reference, respectively. The selection and calculation of integrals from the emission and excitation scattering region and the calculation of absolute PL QY were performed using the FLUORACLE software from the Edinburg Instrument.

FLIM measurements were preformed in confocal configuration in ambient atmosphere on MicroTime200 fluorescence microscope from PicoQuant equipped with 440 nm picosecond laser, 60x objective, PMA Hybrid single photon detector and PicoHarp 300 TCSPC module. The excitation spot size was estimated to 550 nm (FWHM). Based on this value the energy fluences were calculated. Several FLIM pictures can be found in SI (S11–12).

ASSOCIATED CONTENT

Supporting Information

Additional TEM images, PL decays and corresponding fits, tables with fitting parameters, FLIM images.

ACKNOWLEDGMENTS

The authors thank the Sylvia Speller group and Regina Lange for providing the AFM setup. Deutsche Forschungsgemeinschaft (DFG, German Research Foundation) is acknowledged for funding of SFB 1477 "Light-Matter Interactions at Interfaces", project number 441234705. We also acknowledge the European Regional Development Fund of the European Union for funding the PL spectrometer (GHS-20-0035/P000376218) and X-ray diffractometer (GHS-20-0036/P000379642) and the Deutsche Forschungsgemeinschaft (DFG) for funding an electron microscope Jeol NeoARM TEM (INST 264/161-1 FUGG) and an electron microscope ThermoFisher Talos L120C (INST 264/188-1 FUGG).

TABLE OF CONTENTS

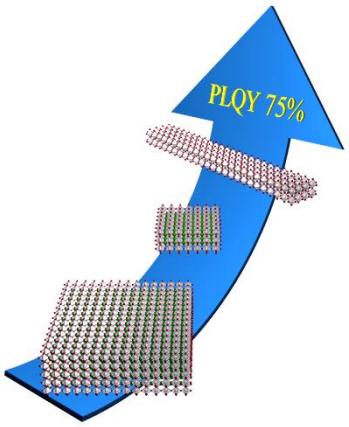

References

[1] Shamsi J, Urban A S, Imran M, Trizio L deand Manna L 2019 *Chemical reviews* **119** 3296.

[2] Correa-Baena J-P, Saliba M, Buonassisi T, Grätzel M, Abate A, Tress Wand Hagfeldt A 2017 *Science* **358** 739.

[3] Blancon J-C, Tsai H, Nie W, Stoumpos C C, Pedesseau L, Katan C, Kepenekian M, Soe C M M, Appavoo Kand Sfeir M Y 2017 *Science* **355** 1288.

[4] Chen J, Zhou Y, Fu Y, Pan J, Mohammed O Fand Bakr O M 2021 *Chemical reviews* **121** 12112.

[5] Carwithen B P *et al.* 2023 *ACS nano* **17** 6638.

[6] Liu X-D, Wang Q, Cheng Z-Q, Qiu Y-H, Zhou Land Wang Q-Q 2017 *Materials Letters* **206** 75.

[7] Teunis M B, Johnson M A, Muhoberac B B, Seifert Sand Sardar R 2017 *Chemistry of Materials* **29** 3526.

[8] Ahmed G H, Yin J, Bose R, Sinatra L, Alarousu E, Yengel E, AlYami N M, Saidaminov M I, Zhang Yand Hedhili M N 2017 *Chemistry of Materials* **29** 4393.

[9] Levchuk I, Osvet A, Tang X, Brandl M, Perea J D, Hoegl F, Matt G J, Hock R, Batentschuk Mand Brabec C J 2017 *Nano letters* **17** 2765.

[10] Weidman M C, Goodman A Jand Tisdale W A 2017 *Chemistry of Materials* **29** 5019.

[11] Hintermayr V A, Richter A F, Ehrat F, Döblinger M, Vanderlinden W, Sichert J A, Tong Y, Polavarapu L, Feldmann Jand Urban A S 2016 *Advanced Materials* **28** 9441.

[12] Klimov V I 2014 *Annu. Rev. Condens. Matter Phys.* **5** 285.

[13] Sun D, Rao Y, Reider G A, Chen G, You Y, Brézin L, Harutyunyan A Rand Heinz T F 2014 *Nano letters* **14** 5625.

[14] Zou W, Li R, Zhang S, Liu Y, Wang N, Cao Y, Miao Y, Xu M, Guo Qand Di D 2018 *Nature communications* **9** 1.

[15] Murawski C, Leo Kand Gather M C 2013 *Advanced Materials* **25** 6801.

[16] Wei K, Zheng X, Cheng X, Shen Cand Jiang T 2016 *Advanced Optical Materials* **4** 1993.

[17] Ahumada-Lazo R, Saran R, Woolland O, Jia Y, Kyriazi M-E, Kanaras A G, Binks Dand Curry R J 2021 *Journal of Physics: Photonics* **3** 21002.

[18] Yuan Land Huang L 2015 *Nanoscale* **7** 7402.

[19] Gramlich M, Bohn B J, Tong Y, Polavarapu L, Feldmann Jand Urban A S 2020 *The journal of physical chemistry letters* **11** 5361.

[20] Villamil Franco C, Mahler B, Cornaggia C, Gustavsson Tand Cassette E 2020 *ACS Applied Nano Materials* **4** 558.

[21] Klein E, Black A, Tokmak Ö, Strelow C, Lesyuk Rand Klinke C 2019 *ACS nano* **13** 6955.

[22] Klein E, Lesyuk Rand Klinke C 2018 *Nanoscale* **10** 4442.

[23] Szafranski Mand Katrusiak A 2016 *The journal of physical chemistry letters* **7** 3458.

[24] Yamada Y, Yamada T, Le Phuong Q, Maruyama N, Nishimura H, Wakamiya A, Murata Yand Kanemitsu Y 2015 *Journal of the American Chemical Society* **137** 10456.

[25] Xing G, Mathews N, Sun S, Lim S S, Lam Y M, Grätzel M, Mhaisalkar Sand Sum T C 2013 *Science* **342** 344.

[26] Wang L, McCleese C, Kovalsky A, Zhao Yand Burda C 2014 *Journal of the American Chemical Society* **136** 12205.

[27] Manser J Sand Kamat P V 2014 *Nature Photonics* **8** 737.

[28] Stamplecoskie K G, Manser J Sand Kamat P V 2015 *Energy & Environmental Science* **8** 208.

[29] Christians J A, Manser J Sand Kamat P V 2015 *The journal of physical chemistry letters* **6** 2086.

[30] Yang Y, Yang M, Li Z, Crisp R, Zhu Kand Beard M C 2015 *The journal of physical chemistry letters* **6** 4688.

[31] Ma Y-Z, Lin H, Du M-H, Doughty Band Ma B 2018 *The journal of physical chemistry letters* **9** 2164.

[32] Ghimire S, Chouhan L, Takano Y, Takahashi K, Nakamura T, Yuyama K-iand Biju V 2018 *ACS Energy Letters* **4** 133.

[33] Kaiser M, Li Y, Schwenzer J, Jakoby M, Allegro I, Gerhard M, Koch M, Ducinskas A, Richards B Sand Graetzel M 2021 *Journal of Applied Physics* **129** 123101.

[34] Fang H-H, Yang J, Adjokatse S, Tekelenburg E, Kamminga M E, Duim H, Ye J, Blake G R, Even Jand Loi M A 2020 *Advanced Functional Materials* **30** 1907979.

[35] Guan Z, Li Y, Zhu Z, Zeng Z, Chen Z, Ren Z, Li G, Tsang S-W, Yip H-Land Xiong Y 2022 *Advanced Functional Materials* **32** 2203962.

[36] Li Y, Allegro I, Kaiser M, Malla A J, Richards B S, Lemmer U, Paetzold U Wand Howard I A 2021 *Materials Today* **49** 35.

[37] Kennedy C L, Hill A Hand Grumstrup E M 2019 *The Journal of Physical Chemistry C* **123** 15827.

[38] Chirvony V S, González-Carrero S, Suarez I, Galian R E, Sessolo M, Bolink H J, Martinez-Pastor J Pand Perez-Prieto J 2017 *The Journal of Physical Chemistry C* **121** 13381.

[39] Eperon G E, Jedlicka Eand Ginger D S 2018 *The journal of physical chemistry letters* **9** 104.

[40] Robel I, Gresback R, Kortshagen U, Schaller R Dand Klimov V I 2009 *Physical review letters* **102** 177404.

[41] D'Innocenzo V, Srimath Kandada A R, Bastiani M de, Gandini Mand Petrozza A 2014 *Journal of the American Chemical Society* **136** 17730.

[42] Yao J-S *et al.* 2020 *The journal of physical chemistry letters* **11** 9371.

[43] Delport G, Chehade G, Lédée F, Diab H, Milesi-Brault C, Trippe-Allard G, Even J, Lauret J-S, Deleporte Eand Garrot D 2019 *The journal of physical chemistry letters* **10** 5153.

[44] Schmidt T, Lischka Kand Zulehner W 1992 *Physical Review B* **45** 8989.

[45] Brenes R, Eames C, Bulović V, Islam M Sand Stranks S D 2018 *Advanced Materials* **30** 1706208.

[46] Fassl P, Zakharko Y, Falk L M, Goetz K P, Paulus F, Taylor A D, Zaumseil Jand Vaynzof Y 2019 *Journal of Materials Chemistry C* **7** 5285.

[47] Chouhan L, Ghimire Sand Biju V 2019 *Angewandte Chemie International Edition* **58** 4875.

[48] Stranks S D, Burlakov V M, Leijtens T, Ball J M, Goriely Aand Snaith H J 2014 *Physical Review Applied* **2** 34007.

[49] Kim H-S, Lee C-R, Im J-H, Lee K-B, Moehl T, Marchioro A, Moon S-J, Humphry-Baker R, Yum J-Hand Moser J E 2012 *Scientific reports* **2** 1.

[50] Huang H, Polavarapu L, Sichert J A, Susha A S, Urban A Sand Rogach A L 2016 *NPG Asia Materials* **8** e328-e328.

[51] Tian W, Zhao C, Leng J, Cui Rand Jin S 2015 *Journal of the American Chemical Society* **137** 12458.

[52] Zheng F, Tan L Z, Liu Sand Rappe A M 2015 *Nano letters* **15** 7794.

[53] Azarhoosh P, McKechnie S, Frost J M, Walsh Aand van Schilfgaarde M 2016 *Apl Materials* **4** 91501.

[54] Munson K T, Kennehan E R, Doucette G Sand Asbury J B 2018 *Chem* **4** 2826.

[55] Leonard A A, Diroll B T, Flanders N C, Panuganti S, Brumberg A, Kirschner M S, Cuthriell S A, Harvey S M, Watkins N Eand Yu J 2023 *ACS nano* **17** 5306.